





Polarization control of epitaxial barium titanate (BaTiO_3) grown by pulsed-laser deposition on a MBE- $\text{SrTiO}_3/\text{Si}(001)$ pseudo-substrate

Cite as: J. Appl. Phys. **128**, 104104 (2020); <https://doi.org/10.1063/5.0019980>

Submitted: 27 June 2020 . Accepted: 25 August 2020 . Published Online: 09 September 2020

Tsang-Hsuan Wang , Po-Chun (Brent) Hsu , Maxim Korytov, Jan Genoe , and Clement Merckling 



View Online



Export Citation



CrossMark

ARTICLES YOU MAY BE INTERESTED IN

[Positive bias temperature instability of \$\text{HfO}_2\$ -based gate stacks at reduced thermal budget for future CMOS technologies](#)

Journal of Applied Physics **128**, 104101 (2020); <https://doi.org/10.1063/5.0006110>

[Critical triple point as the origin of giant piezoelectricity in \$\text{PbMg}_{1/3}\text{Nb}_{2/3}\text{O}_3\$ - \$\text{PbTiO}_3\$ system](#)

Journal of Applied Physics **128**, 104105 (2020); <https://doi.org/10.1063/5.0021765>

[{001}-textured \$\text{Pb}\(\text{Zr}, \text{Ti}\)\text{O}_3\$ thin films on stainless steel by pulsed laser deposition](#)

Journal of Applied Physics **128**, 104103 (2020); <https://doi.org/10.1063/5.0019967>

HIDEN
ANALYTICAL

Instruments for Advanced Science

Contact Hiden Analytical for further details:

W www.HidenAnalytical.com
E info@hiden.co.uk

[CLICK TO VIEW](#) our product catalogue

Gas Analysis

- dynamic measurement of reaction gas streams
- catalysis and thermal analysis
- molecular beam studies
- dissolved species probes
- fermentation, environmental and ecological studies

Surface Science

- UHV TPD
- SIMS
- end point detection in ion beam etch
- elemental imaging - surface mapping

Plasma Diagnostics

- plasma source characterization
- etch and deposition process reaction kinetic studies
- analysis of neutral and radical species

Vacuum Analysis

- partial pressure measurement and control of process gases
- reactive sputter process control
- vacuum diagnostics
- vacuum coating process monitoring



Polarization control of epitaxial barium titanate (BaTiO_3) grown by pulsed-laser deposition on a MBE- $\text{SrTiO}_3/\text{Si}(001)$ pseudo-substrate

Cite as: J. Appl. Phys. **128**, 104104 (2020); doi: [10.1063/5.0019980](https://doi.org/10.1063/5.0019980)

Submitted: 27 June 2020 · Accepted: 25 August 2020 ·

Published Online: 9 September 2020



Tsang-Hsuan Wang,^{1,2,a)} Po-Chun (Brent) Hsu,^{1,3} Maxim Korytov,¹ Jan Genoe,^{1,2} and Clement Merckling¹

AFFILIATIONS

¹Imec, Kapeldreef 75, B-3001 Leuven, Belgium

²ESAT Department, KU Leuven, Kasteelpark Arenberg 10, B-3001 Leuven, Belgium

³Department of Materials Engineering, KU Leuven, Kasteelpark Arenberg 44, B-3001 Leuven, Belgium

^{a)}Author to whom correspondence should be addressed: tsang.hsuan.wang@imec.be

ABSTRACT

Barium titanate (BaTiO_3 or BTO) is a perovskite structure material with interesting intrinsic properties, such as spontaneous ferroelectricity or electro-optical behavior, which strongly depend on thin film crystallinity. For such functional oxide systems, the pulsed-laser deposition (PLD) approach is one promising growth technique due to its precise stoichiometry control of the metals composing the perovskite crystal and higher oxygen environment compared to the classically used molecular beam epitaxy (MBE) approach. In this article, we demonstrate a BTO epitaxial layer by PLD onto an $\text{Si}(001)$ substrate thanks to a thin pseudomorphic SrTiO_3 buffer layer grown by MBE. In our study, the various investigated PLD parameters show strong impacts on the BTO polarization orientation. Hence, adjusting the growth conditions allows control of the polarization orientation, which is crucial for both electronic and optical applications. In addition, lattice parameter changes of BTO layers are investigated using x-ray diffraction and cross-sectional transmission electron microscopy, which evidenced a correlation between mismatch relaxation and oxygen growth pressure. Finally, with the analysis of BTO C-V curves, the polarization direction transition is demonstrated electrically.

Published under license by AIP Publishing. <https://doi.org/10.1063/5.0019980>

INTRODUCTION

Perovskite-based oxide materials are widely studied due to their extensive applications in nanoelectronic, opto-electronic, and electro-mechanic devices.^{1–5} Among these, barium titanate (BaTiO_3 or BTO) attracts much attention due to its strong spontaneous ferroelectricity and notably strong electro-optical properties.^{6–8} At room temperature, BaTiO_3 bulk has a tetragonal crystal symmetry.^{7,9} Upon applying an electric field, the displacement of the titanium atom along the polarization direction generates ferroelectricity and other intriguing properties.^{8,10,11} In order to enhance the ferroelectric behavior, a single-domain BTO layer is required.^{12,13}

BTO thin films with the elongated axis perpendicular to the substrate surface is named c-oriented BTO (c-BTO), while BTO thin films with the elongated axis lying parallel to the substrate surface is named a-oriented BTO (a-BTO). For memory or low-

power switching applications, the c-BTO orientation is preferred due to the ease of fabrication and device design.^{14,15} However, for electro-optical applications, a-BTO orientation is more effective than c-BTO due to its larger Pockels coefficients in such a configuration. As in Pockels tensor of BTO, the largest coefficient is r_{51} , which is at least one order larger than other tensor items.¹⁶ For a more prominent Pockels effect, the applied electric field must lie in the same plane as the optical axis, which can only be achieved by having a-oriented BTO.¹⁷ As a result, controlling the BTO orientation during the epitaxy process is crucial.^{18,19}

For integration of these functional oxides onto silicon substrates, the main techniques used for the epitaxy of such oxide thin films are molecular beam epitaxy (MBE)^{20–22} and pulsed-laser deposition (PLD).^{23–25} MBE is suitable for epitaxial growth due to its slow growth rate and *in situ* reflection high-energy electron diffraction (RHEED) monitoring. Using MBE, epitaxial growth is achieved by the precise control of atomic growth. However, the

limited oxygen environment of maximum 10^{-5} mbar favors the formation of oxygen vacancies in the BTO layer,²⁶ which significantly influence both electrical and optical properties.^{27–29} To reduce the undesirable impact of oxygen vacancies, post-growth annealing at high temperature and especially under high oxygen pressure are needed.^{30,31} However, high temperature annealing results in generally strong interfacial reactions with silicon substrates.^{32,33} Compared to the MBE technique, PLD can reach a higher oxygen pressure of above 10^{-2} mbar based on a different epitaxial process system, including the usage of ceramic target and plasma plume formation between the target and the substrate, giving a very interesting alternative approach for complex oxide epitaxy. Nevertheless, the direct epitaxy of oxides on the Si substrate by PLD is still a challenge due to the higher O_2 pressure, which results in amorphous SiO_2 interface formation, and lack of atomic control.³⁴ Until today, there is only one group that had successfully demonstrated the epitaxial growth of strontium titanate on top of Si(001) substrates using PLD, showing the difficulty of a whole-PLD epitaxial heterostructure.³⁵ To integrate functional oxides on an Si substrate, we then combine these two techniques by using MBE-grown strontium titanate ($SrTiO_3$ or STO) onto the Si substrate as a template,³⁶ followed by a subsequent BTO layer growth with *ex situ* PLD. In this way, we combined the advantages of PLD in stoichiometry and high O_2 pressure together with MBE for the monolithic integration on Si.

Due to the 2% larger lattice parameter compared with STO, the epitaxially grown BTO is initially compressively strained,^{36,37} which results in the elongation of the BTO out-of-plane lattice parameter and hence favors c-BTO growth. Plastic relaxations occurring beyond a critical thickness modify BTO lattice parameters and may impact BTO polarization orientation. In this study, lattice mismatch relaxation behavior inside a BTO film is shown to be closely correlated with PLD parameters, indicating the capability to control the BTO polarization via these growth parameters.

EXPERIMENTAL

The 10-nm-STO buffer layers were grown on an 8-in. Si(001) substrate using the Riber 49 200 mm MBE cluster system. The detailed processes were reported previously.^{36,38} Once we obtained a single-crystalline STO layer, the wafer was then diced into smaller pieces of 3.8×3.8 cm². Note that all BTO films were grown on the same STO batch template to reduce the substrate fluctuation and to strengthen the PLD parameter effects. All BTO films were grown in a Solmates 200 mm production PLD system equipped with a KrF laser and a BTO ceramic target source (99.9%) from Neyco. After introducing the STO/Si samples, the chamber was pumped down to a base pressure at around 10^{-4} mbar; then, the sample holder was heated above 650 °C under oxygen ambient before turning on the laser power. During temperature ramping and the subsequent BTO growth, oxygen gas was introduced, ranging from 0.01 mbar to 0.05 mbar. We confirmed the STO template stability by comparing x-ray diffraction (XRD) peak position and intensity after the 750 °C and low-pressure environment in PLD process. The thickness of all BTO films was kept at around $100 \text{ nm} \pm 10 \text{ nm}$ as measured by the x-ray reflectivity (XRR) analysis. In such analysis, the film thickness was determined by the Fourier transform peak position of the acquired curve.

The epitaxial film crystal quality was further assessed by x-ray diffraction (XRD) for structural analyses. Lattice parameters were calculated by symmetric (002) as well as asymmetric (202) and (022) scans using Bragg's law. Crystal mosaicity can be analyzed by performing the ω -scan of the XRD analysis. We used the full width at half maximum (FWHM) value of the (002) peak by the ω -scan to compare epitaxial film quality. The 10 nm STO buffer layer showed good crystallinity with FWHM of 0.2° – 0.3° . In-plane and out-of-plane lattice parameter distributions were measured with nano-beam diffraction (NBD) using a double-corrected Titan G2 60-300 transmission electron microscope operating at 200 kV. NBD consists of scanning a region of interest with an almost parallel nanometer-size electron beam and acquiring a diffraction pattern in every point.³⁹ The distribution of the local lattice parameter is then calculated by comparing the diffraction patterns acquired in the region of interest with a pattern acquired in a reference unstrained area.⁴⁰ Strain distribution in the two directions perpendicular to the electron beam can be measured with a precision up to 0.1%.⁴¹ Surface roughness was measured by atomic force microscopy (AFM) using Bruker Dimension Edge. C–V measurement was carried out using Agilent E4980A from 1 kHz to 1 MHz and I–V measurement using Agilent B1500A for electrical properties analyses.

RESULTS

Growth rate is one of the most crucial parameters to influence the crystalline quality for an epitaxially grown thin film. In a PLD system, the growth rate is principally controlled by laser parameters. When the laser beam hits the ceramic target, the heat induced by the high-energy laser melts and ablates the materials. The ablated materials include ions, activated molecules, and electrons, forming a plasma plume between the target and the substrate surface. These high-energy species will then diffuse and crystallize on the substrate surface.^{42,43} Pulsed-laser frequency directly influences the growth rate and surface diffusion time, which largely determines the growth mode of thin films, and thus is crucial on improving crystallinity of thin films.⁴⁴ The lower the laser frequency, the lower the growth rate will be as there are no materials being ablated in between pulses. Different laser frequencies were used for BTO growth. Figure 1(a) represents the ω – 2θ scans around the BTO(002) Bragg reflection angle with a varied growth rate between 0.02 nm/s and 0.1 nm/s. The STO(002) peak signal originates from a single-crystalline STO/Si(001) pseudo-substrate. For all samples, a strong peak observed at 44.2° corresponds to the (002) diffraction of the tetragonal BTO crystal. However, for the sample with a growth rate of 0.1 nm/s, additional peaks located at 41.8° and 46.7° were found; these peaks are attributed to the orthorhombic crystal structure of BTO and are present in all samples with a high growth rate (Fig. 1 in the [supplementary material](#)), suggesting the presence of an undesired phase by using a too large growth rate. With a lower laser repetition rate, the atomic diffusion time of species on the substrate surface is increased, allowing better alignment with the initial STO lattice. Therefore, growth rates below 0.1 nm/s lead to the epitaxy of BTO. The epitaxy of BTO is confirmed by BTO(202) and Si(202) φ -scans, which showed the fourfold symmetry and the 45° rotation of BTO lattice on top of Si (Fig. 7 in the [supplementary material](#)). To further assess the

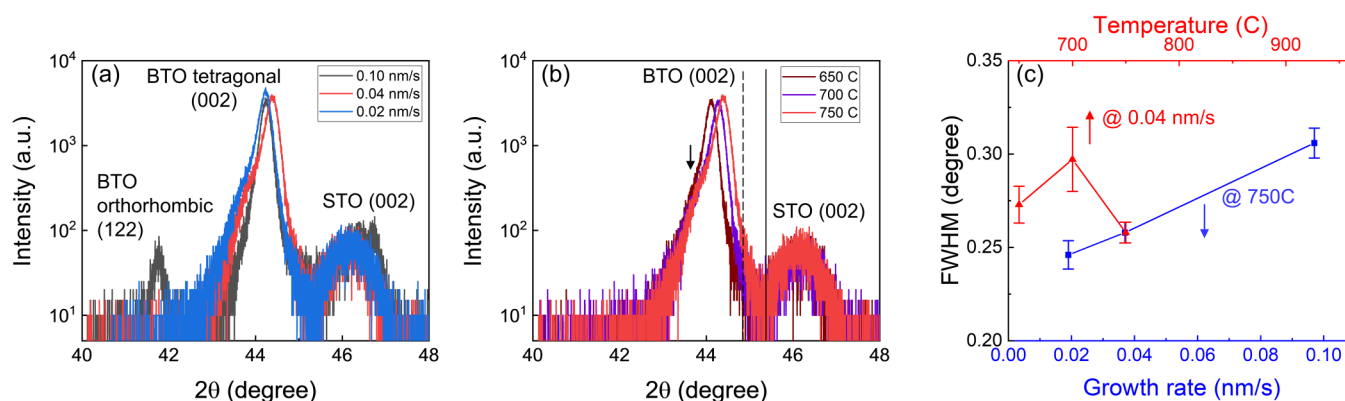


FIG. 1. Symmetric XRD ω - 2θ scan of samples with (a) different growth rates and (b) different substrate temperatures. The arrow indicates the shoulder sub-peak position. The dashed and solid lines represent bulk tetragonal BTO(002) and BTO(200) positions, respectively. All the peak positions are calibrated using the Si(004) peak. (c) The FWHM derived from the (002) ω -scan BTO peak of the samples grown by different growth rates and substrate temperatures.

crystallinity of the different growth rates, the ω -scan of BTO(002) was carried out. In Fig. 1(c), the FWHM values of BTO(002) ω -scan were plotted in the function of growth rate. It can be clearly seen that the crystallinity of BTO films improved as the growth rate reduced with FWHM decreased from around 0.3° to 0.25° .

Epitaxial BTO can be obtained using STO as a buffer layer due to their similar crystal structures and lattice parameters. However, this slight difference of +2% in lattice parameters and +20% in thermal coefficients produces compressive in-plane strain in the BTO epilayer and thus elongates the out-of-plane BTO lattice parameter; on the contrary, the thermal coefficient difference between BTO and Si substrate results in the tensile in-plane strain that shortens the out-of-plane BTO lattice parameter.^{18,37,45} As a result, the BaTiO_3 grown on SrTiO_3 buffer is inherently c-oriented when the thickness is small and gradually becomes a-oriented dominated when increasing the BTO thickness. To change the polarization direction, we need to control the elongated axis orientation, in particular, by enabling a faster strain relaxation mechanism in BTO films. The initial compressive strain can be relaxed by increasing the BTO thickness, or other processing parameters such as the substrate temperature and chamber pressure. By the use of both symmetric and asymmetric XRD scans, we can obtain out-of-plane and in-plane lattice parameters. Upon investigating the XRD peak position and the ratio between the c and a axis, we can know the orientation of the dominant BTO polarization axis.

As shown in Figs. 1(b) and 1(c), increasing the substrate temperature not only improved the crystallinity but also impacted the out-of-plane lattice parameter of the BTO layer. The BTO peak position had shifted to a larger angle with the raising temperature. Also, clear shoulder sub-peaks appeared at a smaller angle next to the main peak in the higher temperature BaTiO_3 case. The dashed and solid lines in the ω - 2θ XRD scan indicate the tetragonal BTO (002) and BTO(200) peak positions, which roughly separate BTO crystal orientations (i.e., polarizations). The real crystal orientations would need to adopt the asymmetric scan results as well.

Compared with the minor shift resulting from the substrate temperature effect, the change in oxygen pressure during BaTiO_3

epitaxy showed more obvious shift, as indicated in Fig. 2(a). The out-of-plane lattice parameter reduced largely as oxygen pressure increased, which we attribute to a gradual change of dominant polarization from c- to a-BTO. Similar to the temperature effect, shoulder sub-peaks appeared next to the BTO(002) main peak. To investigate these shoulder and main peaks, reciprocal space mappings (RSMs) around BTO(002) peak were measured and presented in Fig. 2 in the [supplementary material](#). The FWHM of the main diffraction peak increased from 0.25° to 0.45° , indicating raised mosaicity in the BTO layer, as the oxygen pressure increased. The asymmetric shape of the BTO(002) peak suggested an uneven distribution of the strain inside the high oxygen pressure sample, especially the 0.05 mbar BTO film. The change of lattice parameters with varied oxygen pressures showed to have a similar conclusion with Lyu *et al.*⁴⁶ However, detailed lattice parameter changes were related to the buffer layer, which will be discussed below based on the XRD and NBD results.

Since the main and sub-peaks around BTO(002) indicated different BTO lattice parameters, we further deconvoluted the BTO (002) diffraction peak of each sample and plotted in Figs. 2(b)–2(d). Among different oxygen pressure samples, sub-peak positions were kept fixed for the deconvolution, marked with the same number in Figs. 2(b)–2(d). Shift of the main peak position from smaller angle to larger angle represented the out-of-plane lattice parameter evolution. As illustrated in Fig. 2(e), the area percentage of each peak was compared between different oxygen pressure samples. For the 0.01 mbar low oxygen pressure sample, no presence of shoulder peak indicated a uniform-distributed preferentially c-oriented BTO layer with out-of-plane lattice parameter of $\sim 4.09 \text{ \AA}$. When the oxygen pressure increased to 0.025 mbar, only 17% of the film had the same lattice parameter of 4.09 \AA , while the remaining part of the BTO films had smaller out-of-plane lattice parameters of $\sim 4.06 \text{ \AA}$. We attributed this to mixed c-BTO and a-BTO. This reduction of the lattice parameter was even more pronounced in 0.05 mbar oxygen pressure conditions, with out-of-plane lattice parameter to be 4.03 \AA for almost 60% of the BTO film.

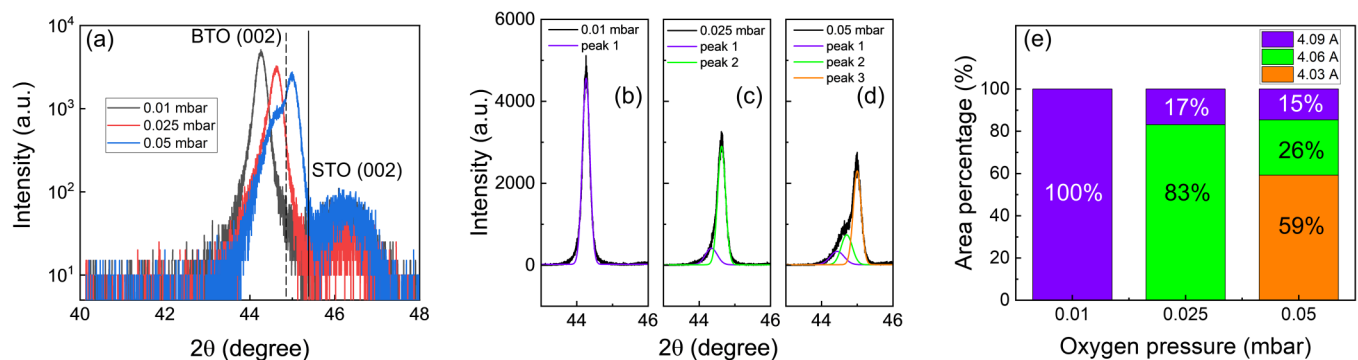


FIG. 2. (a) Symmetric XRD ω -2 θ scan of samples under different oxygen pressures. (b)–(d) Deconvolution of the BTO(002) peak with O_2 pressures of 0.01, 0.025, and 0.05 mbar. (e) Peak area percentage of the deconvoluted peaks. The lattice parameters are calculated by the XRD peak positions using Bragg's law.

The tetragonality of this 0.05 mbar BTO sample was 0.980; hence, we expected that this sample had a dominant a-orientation.

Transmission electron microscopy was used to further investigate the lattice parameter distribution inside the BTO layers grown with different oxygen pressure. Difference of the a and c lattice constants of the tetragonal BTO unit cell is about 1%, so we employed NBD, which is one of the few TEM techniques able to determine such a small variation of the lattice. NBD measured distribution of lattice parameter normalized to a lattice parameter of the reference region. We could not use Si as a reference due to a difference in the lattice orientation of BTO/STO and Si arising from the 45° rotation of their lattices.³⁴ Thus, for the qualitative NBD maps shown in Figs. 3(a)–3(c), we used BTO as a reference region.

Distribution of the in-plane lattice parameter of three samples was quite different [Figs. 3(a)–3(c)]. The sample grown with the lower O_2 pressure [Fig. 3(a)] showed 50–100 nm wide domains. The medium O_2 pressure sample was composed of 30–50 nm wide domains, while the sample grown with higher O_2 pressure showed a very tiny domain structure. These observations were in agreement with the sample surface morphology measured by AFM [Figs. 3(d)–3(f)],

which revealed mosaic structure in all three samples with a lower O_2 pressure sample showing the largest grain size and higher O_2 pressure having the smallest grain size.

The out-of-plane lattice parameter distribution of three samples was rather similar [Figs. 4(a)–4(c)]. However, the sample grown with the lowest O_2 pressure [Fig. 4(a)] showed a bit more uniform distribution of lattice parameter than that of the sample grown with higher O_2 pressure [Fig. 4(c)]. Another difference between the samples was an increase of the out-of-plane lattice parameter next to the BTO/STO interface in the samples grown with high and medium O_2 pressure.

For a quantitative comparison of the lattice parameters between different samples, another set of NBD maps was calculated using STO as a reference region. Averaged profiles traced in the growth direction are shown in Figs. 4(d) and 4(e). In all three samples, the in-plane lattice parameter was rapidly increasing above the interface, indicating that the BTO/STO lattice mismatch was accommodated via the plastic relaxations. We cannot conclude if the BTO layers were fully relaxed or not, but the BTO grown with the lower O_2 pressure had a little bit higher residual strain than two other samples, indicating less mismatch relaxation.

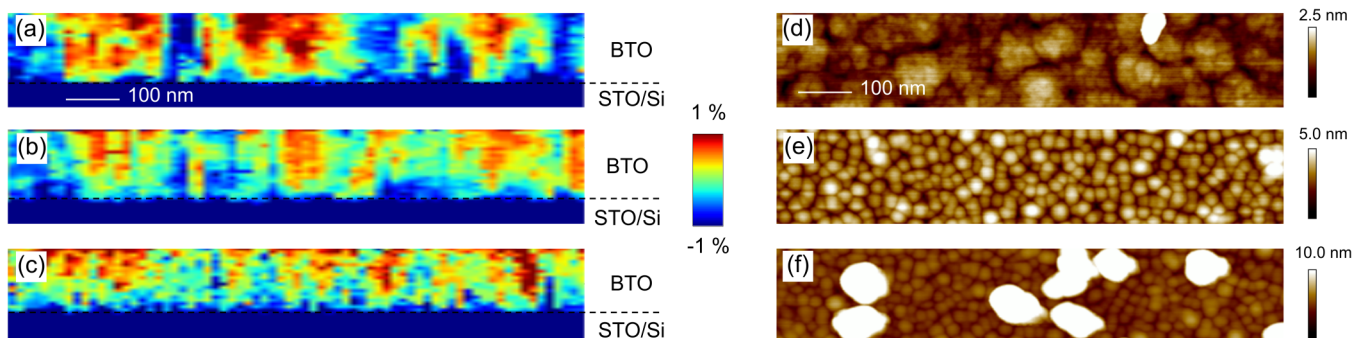


FIG. 3. Cross-sectional NBD maps of in-plane lattice mismatch of (a) c-BTO, (b) mixed BTO, and (c) a-BTO films calculated with the reference region in BTO. AFM surface morphology of (d) c-BTO, (e) mixed BTO, and (f) a-BTO films.

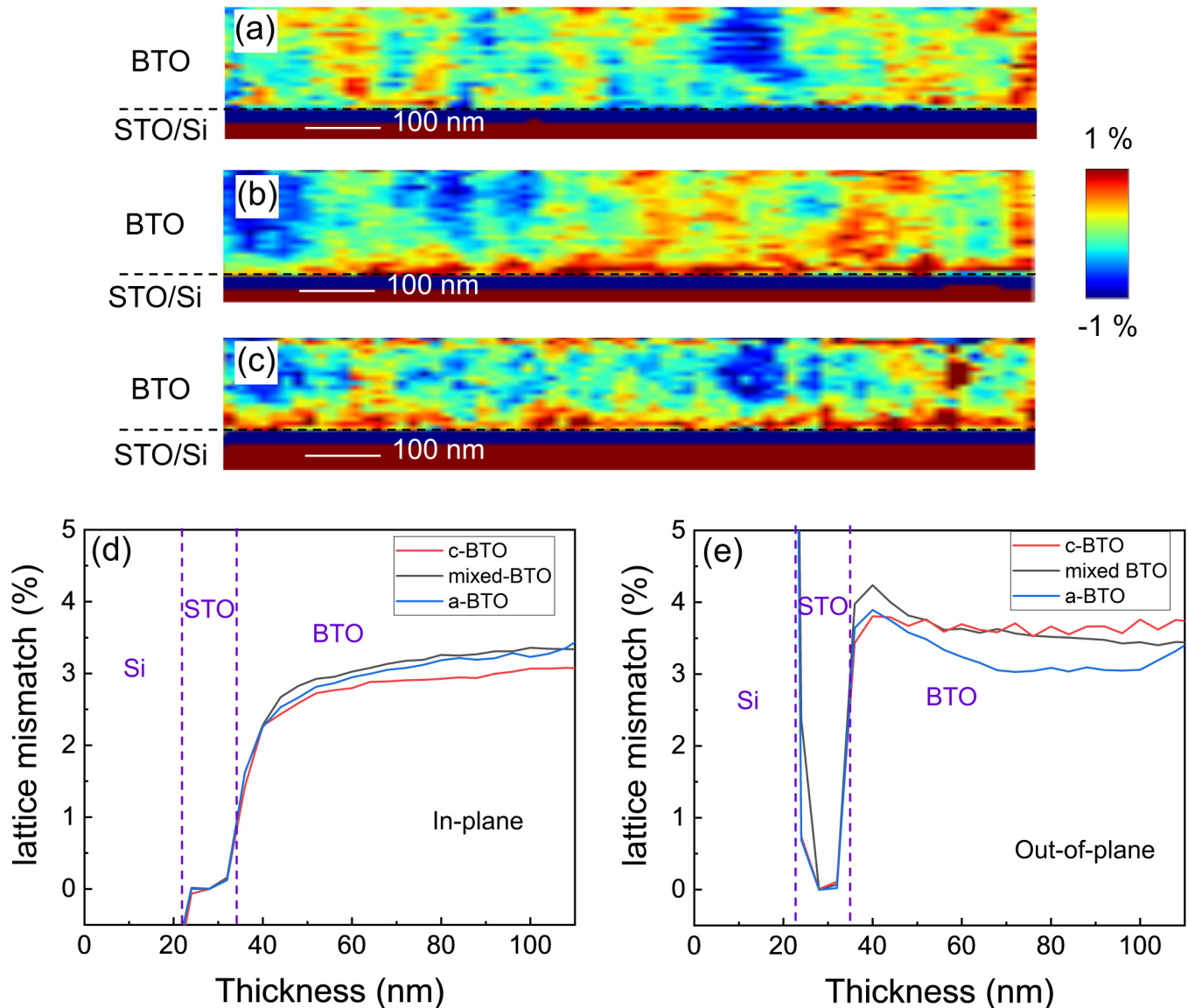


FIG. 4. Cross-sectional NBD maps of out-of-plane lattice mismatch of (a) c-BTO, (b) mixed BTO, and (c) a-BTO films calculated with the reference region in BTO. The averaged lattice mismatch profiles normalized to the STO buffer layer lattice parameter of (d) in-plane and (e) out-of-plane direction.

The out-of-plane lattice parameter of the sample grown with the lower O_2 pressure did not change with the layer thickness, which was in a good agreement with the XRD data showing one peak [see Fig. 2(b)]. The sample with intermediate O_2 pressure had an increased lattice parameter close to the BTO/STO interface and then it gradually decreased, which corresponded to the ω - 2θ scan with two peaks [see Fig. 2(c)]. Similar behavior was observed in the 0.05 mbar sample with the only exception that the lattice parameter increased within the last 15–20 nm of the BTO layer. We could assign three regions of the BTO layers to three peaks of the ω - 2θ

scan curve with the interfacial region corresponding to the highest 4.09 Å out-of-plane lattice parameter, the central part of the layer corresponding to the lower 4.03 Å lattice parameter, and the top part of the layer corresponding to the intermediate lattice parameter 4.06 Å, as measured by XRD. There was also a good agreement between the thickness ratio of these layers and the area percentage of different lattice parameters measured by XRD [Fig. 2(e)]. Interpretation of the XRD and NBD findings will be discussed below.

Electrical characterizations of BTO/STO/ p^+ Si MOS capacitor were investigated with 10 nm Au deposited as top electrodes.

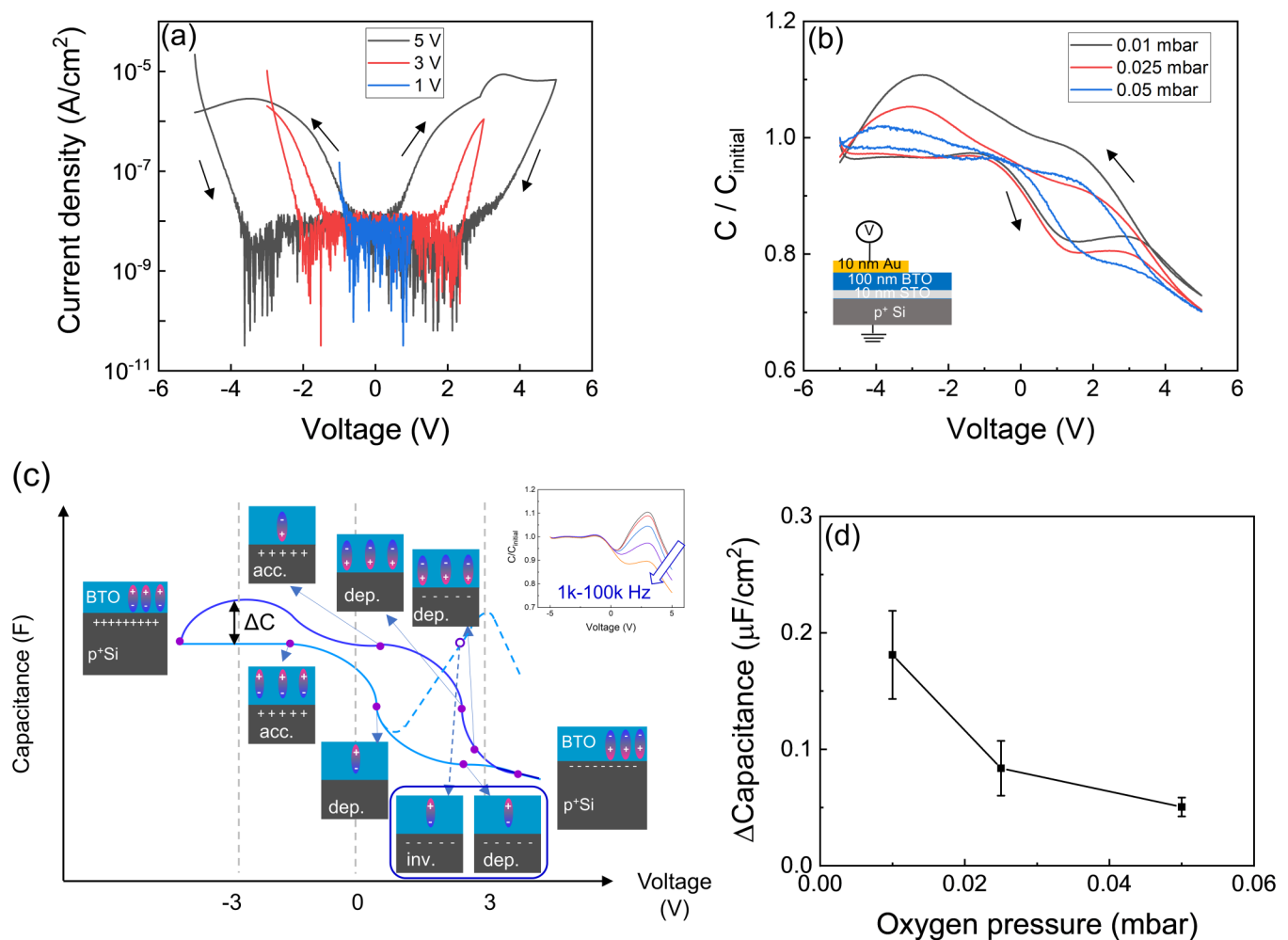


FIG. 5. (a) Current–voltage curve of the 0.01 mbar BTO sample under different voltage biases. Ferroelectric behavior was not shown until applied voltage larger than ± 3 V. (b) Normalized capacitance–voltage curve at 1 MHz of different oxygen pressure samples. The larger the oxygen pressure, the smaller the hysteresis loop observed. (c) The schematic C–V curve, with detailed BTO dipole polarization and STO/ p^+ Si interface charged state being plotted. Inset is multi-frequency C–V measurement from 1 kHz to 100 kHz, which shows a clear inversion layer formation with fixed value of accumulation capacitance. (d) The difference between forward and backward accumulation capacitance for different oxygen pressure samples.

Au electrodes were sputtered and patterned through a shadow mask with a diameter of $200\ \mu\text{m}$. Both I–V and C–V measurements were executed with a p^+ Si substrate grounded and the gate voltage swept from negative to positive bias. Different voltage biases ranged from ± 1 V to ± 5 V were applied during I–V measurements, as shown in Fig. 5(a). For an applied voltage below 2.5 V, no hysteresis behavior was observed; however, the hysteresis loop started to appear at voltages above 3 V and became more pronounced as the applied bias increased. These hysteresis loops are resulted from the ferroelectricity of the BTO film, and the poling electric fields of about $500\ \text{kV/cm}$ also agree with reported values.^{47,48}

C–V measurement was sweeping from negative bias to positive bias, with different voltages ranging from ± 0.5 V to ± 5 V at 1 MHz

frequency. The C–V results showed similar trend as the I–V results, i.e., the hysteresis behavior became prominent when the voltage bias was larger than 3 V (Fig. 3 in the [supplementary material](#)). As shown in Fig. 5(b), counterclockwise hysteresis loops were observed in all the different oxygen pressure samples and was most notable in the 0.01 mbar BTO, which showed the largest hysteresis loop. Backward curve showed a positive flatband voltage shift and different capacitance at accumulation/depletion regions compared with the forward curve, which can be understood by the charge and poling effect in BTO, as illustrated in Fig. 5(c). When the BTO layers were biased with -5 V, the dipoles inside the BTO film were polarized up toward the top contact due to the large enough electric field. At the same time, the capacitor was at the accumulation

region with excess positive charges accumulated at the BTO/Si interface. As the bias increased toward zero, the accumulated charges at the BTO/Si interface as well as the voltage stressed at BTO decreased, resulting in less polarized-up dipoles inside BTO films until the flat-band voltage was reached. After the flatband voltage, the positive bias drop mainly depleted the p-type silicon, with little voltage change crossing the BTO film. Thus, polarized-up dipoles remained unchanged, and the C-V curve was behaving like normal depleted MOS. However, dipoles were polarized down after +3 V with a reverse direction due to the strong inversion layer formation, resulting in an even lower capacitance value. To confirm the inversion layer formation, multi-frequency (MULTI-F) C-V from 1 kHz to 100 kHz were measured and plotted in the inset of Fig. 5(c). An obvious inversion region formation at ~1 kHz with a fixed value of accumulation capacitance at full range of frequency can be clearly observed, which was consistent to a MULTI-F C-V curve of a normal p-Si MOS capacitor. A more detailed result and explanation of MULTI-F C-V hysteresis can be found in Fig. 4 in the [supplementary material](#). Based on the results, a dotted line in the schematics indicated the low frequency curve, in comparison with the solid line for C-V curve at 1 MHz. For the backward curve, a similar but reverse poling direction inside BTO films resulted in the shift of flatband voltage and the capacitance difference. When the applied voltage was smaller than -3 V, dipoles were again polarized up reversely and lowered the accumulation capacitance, ending the backward curve with the same value as the forward curve at -5 V.

At the parallel mode of C-V measurement, the measuring capacitance at accumulation bias might be described as follows:⁴⁹

$$C_{meas}^{-1} \propto \left(\frac{\epsilon'_{eff,BTO}}{t_{BTO}} \right)^{-1} + \left(\frac{\epsilon'_{STO}}{t_{STO}} \right)^{-1}. \quad (1)$$

$\epsilon'_{eff,BTO}$ is the real part of BTO permittivity and ϵ'_{STO} is the real part of STO permittivity, which should be a constant since no ferroelectricity existed in cubic STO. $t_{BTO,STO}$ are the BTO and STO thickness, respectively. Because the dipole polarizability of BTO can respond below microwave frequency (~GHz) and $t_{BTO,STO}$ is the same for all the samples, C_{meas} at the accumulation should represent the value of $\epsilon'_{eff,BTO}$. Furthermore, it should also give the number of c-BTO dipoles because the (001)-axis electrical field only triggers the spontaneous polarization in c-BTO instead of a-BTO.⁵⁰ Since BTO is a ferroelectric material, the dielectric constant ϵ' is the largest at the coercive point, which is at ± 3 V in our device.⁵¹ Based on Eq. (1), the backward curve at the coercive point (at -3 V) had larger $\epsilon'_{eff,BTO}$ than the forward curve, resulting in a higher C_{meas} . Therefore, the capacitance difference values were linked with (001)-dipoles and were extracted in Fig. 5(d). As oxygen pressure increased, the capacitance difference was reduced, which also linked to the smaller hysteresis behavior in Fig. 5(b). Based on the C-V characteristics, the dielectric constant at low frequencies (i.e., 100 kHz) was extracted with an average value of 130, which was in good agreement with reported values of epitaxial BTO.^{52,53} For the 0.05 mbar sample, even though it was mostly a-oriented from the XRD result, the BTO close to the STO layer with thickness around 20 nm was still c-oriented. Thus, the hysteresis

loop was still measured but smaller than 0.01 mbar BTO due to the less number of dipoles along the (001) direction. The BTO C-V curve can be nicely explained via the dipole amount and direction, and showed good agreement with XRD results, and is therefore an electrical demonstration of a c- to a-transition with the oxygen pressure variation.

DISCUSSION

Our experimental study showed that the growth conditions made a drastic impact on the structural and electrical properties of the BTO layers. XRD indicated that the dominant orientation of the BTO polarization could be changed from c to a by increasing the O₂ pressure. Due to the similar thickness between BTO samples, the peak position shift should only result from different degree of lattice mismatch relaxations inside the BTO thin films by changing the growth parameters. In addition, the presence of sub-peaks in XRD plots of high and medium O₂ pressure samples suggested a non-uniform distribution of lattice inside these samples.

NBD analysis revealed a mosaic structure of three samples and highlighted differences in the mosaicity between the samples. The low O₂ pressure sample had the largest domain size and also showed higher lattice mismatch than two other samples. We attributed the accelerated relaxation process in the medium and high O₂ pressure samples to the reduction of the BTO domain size, which facilitated strain relaxation via domain formation.⁵⁴ With a larger domain size inside the low O₂ pressure sample, the strain relaxation might be delayed compared with the smaller domain size samples. The residual compressive strain in the low O₂ pressure sample produced elongation of the out-of-plane lattice parameter, favoring growth of c-BTO.

Observed differences in the grain size and strain relaxation could also be related to the growth mode change. As we increased the oxygen pressure, the BTO films tended to favor 3D growth, as shown in the AFM images in Figs. 3(d)–3(f). BTO clusters appeared when oxygen pressure increased to 0.05 mbar. The difference in the growth mode can also explain the observed difference in strain relaxation since the formation of the misfit dislocations at the grain boundaries during 3D growth occurs easier than during 2D growth, which requires dislocation gliding.

Another possible explanation for the delayed strain relaxation of the low oxygen pressure sample was the amount of oxygen vacancies. Oxygen vacancies inside perovskite systems were reported to have an impact on the strain relaxation behavior. In LaSrCoO (LSCO) material system, oxygen vacancies helped retain strain inside these perovskite oxide films by re-ordering on Co–O planes.^{55–57} With this re-ordering, strain was not relaxed until even larger thickness was reached. In our BTO/STO/Si system, the strain behavior could be explained with the similar assumption. For samples grown with lower oxygen pressure, more oxygen vacancies were expected inside the as-deposited thin films. However, this oxygen vacancies re-ordering is not yet reported inside the BTO material; thus, more studies would need to be carried out before making a solid conclusion.

Piezoelectric force microscopy (PFM) is a widely used technique for ferroelectricity characterization with the ability to analyze the domain and dipole behavior in the out-of-plane direction.

However, for the in-plane domain, i.e., the a-BTO, the characterization is not feasible due to the perpendicular electric field direction with respect to the in-plane dipoles. Compared with PFM, C–V measurement uses a similar concept by measuring charge differences in the BTO. In addition, we can further extract the dielectric constant from the C–V curves, which is another indication of film quality and can also be linked with the optical indices.

The C–V hysteresis can be correlated with both the charge defects and the ferroelectric behavior of the BTO films. However, the positively charged oxygen vacancies and the ferroelectricity result in a different direction of hysteresis loop. In our C–V curve, the counterclockwise direction indicates that the ferroelectricity is more pronounced than the charged defect. Thus, for our BTO films, it will be difficult to use C–V measurement for charged defect characterization.

CONCLUSION

In conclusion, we demonstrate an epitaxial BTO film growing on a top STO/Si(001) pseudo-substrate by the PLD technique. Adjusting oxygen pressure during growth results in polarization direction change. The lattice mismatch relaxation process is measured using XRD and confirmed by cross-sectional NBD analysis. By measuring electrical properties of ferroelectric BTO films, the hysteresis behavior is explained and again well-matched with XRD results.

SUPPLEMENTARY MATERIAL

See the [supplementary material](#) for the additional XRD and C–V hysteresis results.

ACKNOWLEDGMENTS

This research has received funding from the European Research Council (ERC) under the European Union's Horizon 2020 Research and Innovation Program (Grant Agreement No. 742299).

DATA AVAILABILITY

The data that support the findings of this study are available from the corresponding author upon reasonable request.

REFERENCES

- ¹X. Zhu, Z. Liu, and N. Ming, *J. Mater. Chem.* **20**, 4015 (2010).
- ²D. Panda and T.-Y. Tseng, *Ferroelectrics* **471**, 23 (2014).
- ³T. Yajima, Y. Hikita, and H. Y. Hwang, *Nat. Mater.* **10**, 198 (2011).
- ⁴C. Xiong, W. H. P. Pernice, J. H. Ngai, J. W. Reiner, D. Kumah, F. J. Walker, C. H. Ahn, and H. X. Tang, *Nano Lett.* **14**, 1419 (2014).
- ⁵D. Damjanovic, P. Muralt, and N. Setter, *IEEE Sens. J.* **1**, 191 (2001).
- ⁶A. J. Moulson and J. M. Herbert, *Electroceramics* (Wiley, 2003).
- ⁷H. D. Megaw, *Acta Crystallogr.* **5**, 739 (1952).
- ⁸S. Abel, T. Stöferle, C. Marchiori, C. Rossel, M. D. Rossell, R. Erni, D. Caimi, M. Sousa, A. Chelnokov, B. J. Offrein, and J. Fompeyrine, *Nat. Commun.* **4**, 1671 (2013).
- ⁹C. Eischenschmidt, H. T. Langhammer, R. Steinhausen, and G. Schmidt, *Ferroelectrics* **432**, 103 (2012).
- ¹⁰A. Petraru, J. Schubert, M. Schmid, and C. Buchal, *Appl. Phys. Lett.* **81**, 1375 (2002).
- ¹¹H. A. Lu, L. A. Wills, B. W. Wessels, W. P. Lin, and G. K. Wong, *Appl. Phys. Lett.* **63**, 874 (1993).
- ¹²K. J. Kormondy, Y. Popoff, M. Sousa, F. Eltes, D. Caimi, M. D. Rossell, M. Fiebig, P. Hoffmann, C. Marchiori, M. Reinke, M. Trassin, A. A. Demkov, J. Fompeyrine, and S. Abel, *Nanotechnology* **28**, 75706 (2017).
- ¹³S. Abel, F. Eltes, J. E. Ortmann, A. Messner, P. Castera, T. Wagner, D. Urbonas, A. Rosa, A. M. Gutierrez, D. Tulli, P. Ma, B. Baeuerle, A. Josten, W. Heni, D. Caimi, L. Czornomaz, A. A. Demkov, J. Leuthold, P. Sanchis, and J. Fompeyrine, *Nat. Mater.* **18**, 42 (2019).
- ¹⁴L. Mazet, S. M. Yang, S. V. Kalinin, S. Schamm-Chardon, and C. Dubourdieu, *Sci. Technol. Adv. Mater.* **16**, 036005 (2015).
- ¹⁵M. Scigaj, C. H. Chao, J. Gázquez, I. Fina, R. Moalla, G. Saint-Girons, M. F. Chisholm, G. Herranz, J. Fontcuberta, R. Bachelet, and F. Sánchez, *Appl. Phys. Lett.* **109**, 122903 (2016).
- ¹⁶R. W. Boyd, *Nonlinear Optics* (Academic Press, Burlington, 2008), pp. 511–541.
- ¹⁷P. Castera, D. Tulli, A. M. Gutierrez, and P. Sanchis, *Opt. Express* **23**, 15332 (2015).
- ¹⁸V. Vaithyanathan, J. Lettieri, W. Tian, A. Sharan, A. Vasudevarao, Y. L. Li, A. Kochhar, H. Ma, J. Levy, P. Zschack, J. C. Woicik, L. Q. Chen, V. Gopalan, and D. G. Schlom, *J. Appl. Phys.* **100**, 024108 (2006).
- ¹⁹C. Schmitz-Antoniak, D. Schmitz, P. Borisov, F. M. F. de Groot, S. Stienen, A. Warland, B. Krumme, R. Feyerherm, E. Dudzik, W. Kleemann, and H. Wende, *Nat. Commun.* **4**, 2051 (2013).
- ²⁰S.-H. Baek and C.-B. Eom, *Acta Mater.* **61**, 2734 (2013).
- ²¹R. Droopad, Z. Yu, H. Li, Y. Liang, C. Overgaard, A. Demkov, X. Zhang, K. Moore, K. Eisenbeiser, M. Hu, J. Curless, and J. Finder, *J. Cryst. Growth* **251**, 638 (2003).
- ²²C. Merckling, G. Saint-Girons, C. Botella, G. Hollinger, M. Heyns, J. Dekoster, and M. Caymax, *Appl. Phys. Lett.* **98**, 092901 (2011).
- ²³H. Guo, D. Sun, W. Wang, Z. Gai, I. Kravchenko, J. Shao, L. Jiang, T. Z. Ward, P. C. Snijders, L. Yin, J. Shen, and X. Xu, *J. Appl. Phys.* **113**, 234301 (2013).
- ²⁴G. Koster, G. J. H. M. Rijnders, D. H. A. Blank, and H. Rogalla, *Appl. Phys. Lett.* **74**, 3729 (1999).
- ²⁵H. M. Christen and G. Eres, *J. Phys. Condens. Matter* **20**, 264005 (2008).
- ²⁶P. G. Sundell, M. E. Björketun, and G. Wahnström, *Phys. Rev. B* **73**, 104112 (2006).
- ²⁷H. N. Lee, S. S. Ambrose Seo, W. S. Choi, and C. M. Rouleau, *Sci. Rep.* **6**, 19941 (2016).
- ²⁸E. Hildebrandt, J. Kurian, M. M. Miller, T. Schroeder, H. J. Kleebe, and L. Alff, *Appl. Phys. Lett.* **99**, 112902 (2011).
- ²⁹J. Seidel, P. Maksymovych, Y. Batra, A. Katan, S. Y. Yang, Q. He, A. P. Baddorf, S. V. Kalinin, C. H. Yang, J. C. Yang, Y. H. Chu, E. K. H. Salje, H. Wormeester, M. Salmeron, and R. Ramesh, *Phys. Rev. Lett.* **105**, 197603 (2010).
- ³⁰M. E. Zvanut, S. Jeddy, E. Towett, G. M. Janowski, C. Brooks, and D. Schlom, *J. Appl. Phys.* **104**, 064122 (2008).
- ³¹H. Y. Xu, Y. H. Huang, S. Liu, K. W. Xu, F. Ma, and P. K. Chu, *RSC Adv.* **6**, 79383 (2016).
- ³²B. J. Fishbein, *J. Electrochem. Soc.* **134**, 674 (1987).
- ³³S. Choi, K. H. Min, M. S. Jeong, J. I. Lee, M. G. Kang, H.-E. Song, Y. Kang, H.-S. Lee, D. Kim, and K.-H. Kim, *Sci. Rep.* **7**, 12853 (2017).
- ³⁴T. Tambo, T. Nakamura, K. Maeda, H. Ueba, and C. Tatsuyama, *Jpn. J. Appl. Phys.* **37**, 4454 (1998).
- ³⁵M. Spreitzer, D. Klement, R. Egoavil, J. Verbeeck, J. Kovač, A. Založnik, G. Koster, G. Van Tendeloo, D. Suvorov, and G. Rijnders, *J. Mater. Chem. C* **8**, 518 (2020).
- ³⁶C. Merckling, M. Korytov, U. Celano, M.-H. M. Hsu, S. M. Neumayer, S. Jesse, and S. de Gendt, *J. Vac. Sci. Technol. A* **37**, 021510 (2019).
- ³⁷F. Niu and B. W. Wessels, *J. Vac. Sci. Technol. B* **25**, 1053 (2007).
- ³⁸M.-H. M. Hsu, A. Marinelli, C. Merckling, M. Pantouvaki, J. Van Campenhout, P. Absil, and D. Van Thourhout, *Opt. Mater. Express* **7**, 2030 (2017).
- ³⁹J. M. Cowley, *Ultramicroscopy* **90**, 197 (2002).
- ⁴⁰P. Favia, M. Bargallo Gonzales, E. Simoen, P. Verheyen, D. Klenov, and H. Bender, *J. Electrochem. Soc.* **158**, H438 (2011).

- ⁴¹D. Cooper, T. Denneulin, N. Bernier, A. Béché, and J.-L. Rouvière, *Micron* **80**, 145 (2016).
- ⁴²J. Z. Tischler, G. Eres, B. C. Larson, C. M. Rouleau, P. Zschack, and D. H. Lowndes, *Phys. Rev. Lett.* **96**, 226104 (2006).
- ⁴³H. Schraknepper, C. Bäumer, F. Gunkel, R. Dittmann, and R. A. De Souza, *APL Mater.* **4**, 126109 (2016).
- ⁴⁴C. W. Schneider and T. Lippert, in *Laser Process. Material*, edited by P. Schaaf (Springer, Berlin, 2010), pp. 89–112.
- ⁴⁵M.-H. M. Hsu, D. Van Thourhout, M. Pantouvaki, J. Meersschaut, T. Conard, O. Richard, H. Bender, P. Favia, M. Vila, R. Cid, J. Rubio-Zuazo, G. R. Castro, J. Van Campenhout, P. Absil, and C. Merckling, *Appl. Phys. Express* **10**, 065501 (2017).
- ⁴⁶J. Lyu, S. Estandía, J. Gazquez, M. F. Chisholm, I. Fina, N. Dix, J. Fontcuberta, and F. Sánchez, *ACS Appl. Mater. Interfaces* **10**, 25529 (2018).
- ⁴⁷M. Scigaj, N. Dix, I. Fina, R. Bachelet, B. Warot-Fonrose, J. Fontcuberta, and F. Sánchez, *Appl. Phys. Lett.* **102**, 112905 (2013).
- ⁴⁸O. Trithaveesak, J. Schubert, and C. Buchal, *J. Appl. Phys.* **98**, 114101 (2005).
- ⁴⁹J. Tao, C. Z. Zhao, C. Zhao, P. Taechakumput, M. Werner, S. Taylor, and P. R. Chalker, *Materials* **5**, 1005 (2012).
- ⁵⁰D. J. Griffiths, *Introduction to Electrodynamics*, 4th ed. (Cambridge University Press, Cambridge, 2019), pp. 167–209.
- ⁵¹D. Damjanovic, *Rep. Prog. Phys.* **61**, 1267 (1998).
- ⁵²G. Niu, B. Gautier, S. Yin, G. Saint-Girons, P. Lecoeur, V. Pillard, G. Hollinger, and B. Vilquin, *Thin Solid Films* **520**, 4595 (2012).
- ⁵³V. Srikant, E. J. Tarsa, D. R. Clarke, and J. S. Speck, *J. Appl. Phys.* **77**, 1517 (1995).
- ⁵⁴B. S. Kwak, A. Erbil, J. D. Budai, M. F. Chisholm, L. A. Boatner, and B. J. Wilkens, *Phys. Rev. B* **49**, 14865 (1994).
- ⁵⁵J. Gazquez, S. Bose, M. Sharma, M. A. Torija, S. J. Pennycook, C. Leighton, and M. Varela, *APL Mater.* **1**, 012105 (2013).
- ⁵⁶J. Gazquez, W. Luo, M. P. Oxley, M. Prange, M. A. Torija, M. Sharma, C. Leighton, S. T. Pantelides, S. J. Pennycook, and M. Varela, *Nano Lett.* **11**, 973 (2011).
- ⁵⁷D. O. Klenov, W. Donner, B. Foran, and S. Stemmer, *Appl. Phys. Lett.* **82**, 3427 (2003).